Key Points:
- Fracture dissolution patterns are insensitive to the initial aperture distribution
- Wormhole competition leads to patterns where the wormhole spacing is comparable to the length
- Localized regions of high permeability (vugs) can be overwhelmed by spontaneous wormhole formation

Initial conditions or emergence: What determines dissolution patterns in rough fractures?

Virat K. Upadhyay[1], Piotr Szymczak[2], and Anthony J. C. Ladd[1]

[1]Department of Chemical Engineering, University of Florida, Gainesville, Florida, USA, [2]Institute of Theoretical Physics, Faculty of Physics, University of Warsaw, Warsaw, Poland

Abstract Dissolution of fractured rocks is often accompanied by the formation of highly localized flow paths. While the fluid flow follows existing fractures in the rock, these fissures do not, in general, open uniformly. Simulations and laboratory experiments have shown that distinct channels or "wormholes" develop within the fracture, from which a single highly localized flow path eventually emerges. The aim of the present work is to investigate how these emerging flow paths are influenced by the initial aperture field. We have simulated the dissolution of a single fracture starting from a spatially correlated aperture distribution. Our results indicate a surprising insensitivity of the evolving dissolution patterns and flow rates to the amplitude and correlation length characterizing the imposed aperture field. We connect the similarity in outcomes to the self-organization of the flow into a small number of wormholes, with the spacing determined by the length of the longest wormholes. We have also investigated the effect of a localized region of increased aperture on the developing dissolution patterns. A competition was observed between the tendency of the high-permeability region to develop the dominant wormhole and the tendency of wormholes to spontaneously nucleate throughout the rest of the fracture. We consider the consequences of these results for the modeling of dissolution in fractured and porous rocks.

1. Introduction

In general, modeling physical or chemical processes requires a complete knowledge of the state of the system at some earlier point in time. This is problematic in geological systems where much of the initial state of the Earth is hidden from view and can only be determined by inference. On the other hand, there are many examples of nonlinear systems [*Meakin*, 1998; *Jamtveit and Hammer*, 2012] in which patterns are formed spontaneously, with intrinsic length scales that are independent of initial conditions. It is therefore of interest if predictions can be made about the evolution of geological formations without making explicit reference to the initial conditions. In general, the relative importance of noise, initial fluctuations, and intrinsic instability in pattern formation is complex [*Stanley and Ostrowsky*, 1988]. For example, in columnar growth [*Meakin and Krug*, 1992; *Krug et al.*, 1993], the final distribution of the growing columns can be either dependent or independent of the initial noise, depending on the particulars of the growth process. The investigation reported in this paper focuses on pattern formation during the dissolution of a single fracture, where the flow spontaneously focuses itself in dissolution channels or "wormholes." We have systematically varied the statistical properties of the initial aperture field, so that the homogenization scale varies by nearly 3 orders of magnitude. At long times, we find that the distribution of wormholes within the fracture is almost independent of the initial aperture field.

Petroleum engineers first noticed that the permeability increase around a wellbore during acidization depended in a nonmonotonic way on flow rate [*Rowan*, 1959], with the maximum corresponding to the spontaneous development of highly localized flow paths, or wormholes. Subsequently, wormhole formation was investigated in the laboratory using a variety of materials, for example, plaster dissolved by water [*Ewers*, 1982; *Daccord*, 1987], acidized limestone cores [*Hoefner and Fogler*, 1988; *Fredd and Fogler*, 1998; *Polak et al.*, 2004; *Luquot and Gouze*, 2009; *Noiriel et al.*, 2013; *Luquot et al.*, 2014], transparent KH_2PO_4 crystals [*Detwiler et al.*, 2003; *Detwiler*, 2010], and salt [*Kelemen et al.*, 1995; *Golfier et al.*, 2002]. Different dissolution regimes were identified, depending on the flow rate in the sample [*Hoefner and Fogler*, 1988; *Fredd and Fogler*, 1998; *Golfier et al.*, 2002]. At low flow rates, dissolution was limited to a region near the inlet, whereas at high flow rates the sample dissolved uniformly; wormhole formation was observed at intermediate flow rates.
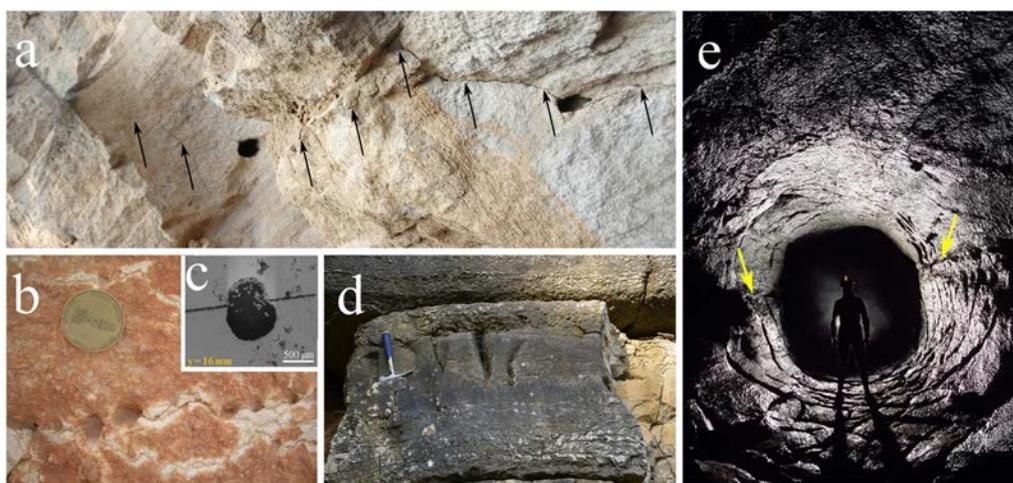
Figure 1. Examples of nonuniform fracture dissolution accompanied by wormhole formation. (a) A fractured wall (marked by black arrows) at a limestone quarry in Smerdyna, Poland. Two wormholes have developed along the width of the fracture; the one on the left is 11 cm in diameter. (b) Wormholes formed at the inlet of a vertical joint in the limestone quarry near Katowice, Poland (photo courtesy of Daniel Koehn, University of Glasgow). (c) Wormhole at the outlet of a fractured limestone core flushed with a CO_2-rich solution (courtesy of María García Ríos and Linda Luquot, Technical University of Catalonia) [*García Ríos*, 2015]. (d) A dissolutionally enlarged styolite with several wormholes in a limestone wall of Mitzpe Ramon quarry, Israel (photo courtesy of Paweł Kondratiuk, University of Warsaw). (e) A conduit in a phreatic cave in Dan Yr Ogof, Swansea Valley, South Wales. The yellow arrows mark the initial fissure (photo courtesy of Brendan Marris, Dudley Caving Club).

Understanding the processes underlying wormhole formation and development remains an important problem for the petroleum engineering community [*Panga et al.*, 2005; *Cohen et al.*, 2008; *Maheshwari and Balakotaiah*, 2013; *Ishibashi et al.*, 2013], usually with the aim of optimizing reservoir acidization. In recent years, further research has been initiated because of the relevance of wormhole formation to CO_2 sequestration [*Luquot and Gouze*, 2009; *Ellis et al.*, 2011; *Elkhoury et al.*, 2013; *Hao et al.*, 2013; *Deng et al.*, 2013; *Carroll et al.*, 2013; *Smith et al.*, 2013; *Elkhoury et al.*, 2015; *Ott and Oedai*, 2015]. Since many of the potential reservoirs for CO_2 storage are in carbonate strata, it is crucial to understand how the flow of CO_2-acidified brine impacts the long-term changes in porosity and permeability of the reservoirs, and how it affects the caprock properties. Finally, elucidation of wormhole dynamics in dissolving fractures is important in understanding a number of karst processes, such as cave and solution tube formation, as well as the denudation of hydraulic structures [*Hanna and Rajaram*, 1998; *Cheung and Rajaram*, 2002; *Szymczak and Ladd*, 2011a; *Oltean et al.*, 2013; *Chaudhuri et al.*, 2013].

It has been established theoretically that the dissolution of a porous matrix is unstable to infinitesimal perturbations in the porosity field [*Chadam et al.*, 1986; *Ortoleva et al.*, 1987]. The dissolution regimes observed in the laboratory can be understood within the framework of linear stability analysis [*Szymczak and Ladd*, 2014] by noting that the penetration length l_p (the scale over which the concentration decays) has two different limiting behaviors [*Szymczak and Ladd*, 2013]: at low flow rates $l_p \sim D/v_0$ (D is the diffusion coefficient, and v_0 is the characteristic velocity of the flow), whereas at high flow rates $l_p \sim v_0\tau$, where τ is the characteristic time scale for the dissolution reaction. In this context, a low flow rate means $v_0 \ll \sqrt{D/\tau}$ whereas a high flow rate corresponds to $v_0 \gg \sqrt{D/\tau}$. A linear stability analysis of transport-limited dissolution ($v_0 \ll \sqrt{D/\tau}$) [*Ortoleva et al.*, 1987] shows that there is a minimum wavelength $\lambda_{min} \sim l_p$ for an instability to grow. When D/v_0 becomes comparable to the dimensions of the system, the planar front is stable and penetration is limited to the region near the inlet. At larger velocities the front becomes unstable [*Chadam et al.*, 1986], and this instability leads to the development of wormholes. At still larger velocities, l_p increases with velocity (as $v_0\tau$) and eventually becomes comparable to the length of the system; at this point wormhole formation is overtaken by uniform dissolution.

A stability analysis of the dissolution front in an initially uniform fracture [*Szymczak and Ladd*, 2011b, 2012] reveals some important distinctions from the more familiar case of a porous matrix. In fact, there are two separate instabilities in the dissolution of a porous matrix. The most commonly studied instability
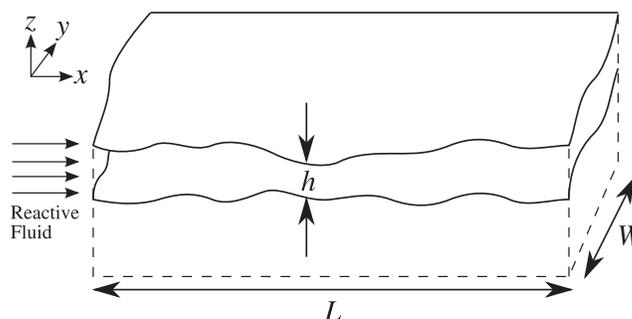
Figure 2. Dissolution of a rough fracture of length L and width W. Fluid flow is in the x direction, and the fracture surfaces dissolve in the normal (z) direction. The aperture $h(x, y)$ is the distance between the fracture surfaces.

[*Chadam et al.*, 1986; *Ortoleva et al.*, 1987; *Szymczak and Ladd*, 2014] occurs when there is a steadily propagating front separating the dissolved and undissolved regions, but the dissolution of an entirely uniform porous matrix (before the front even develops) is also unstable [*Szymczak and Ladd*, 2011b]. Fracture dissolution is similar to this second instability because the aperture opens without limit (in essence) and there is then no propagating front. The stability analysis for a uniform fracture indicates that all wavelengths are unstable, although there is a strong selection in favor of wavelengths that are of the same scale as the penetration length [*Szymczak and Ladd*, 2011a]. Thus, the front is unstable at low velocities, and there is no range of flow rates where the dissolution is limited to the inlet; although its growth rate may be small, eventually an instability will always develop. Nevertheless, at sufficiently high flow rates ($v_0 \gg \sqrt{Dr/\tau}$) it remains possible for fractures to dissolve uniformly, once the penetration length approaches the dimensions of the system.

Once perturbations in a planar front develop, they quickly grow into wormholes which advance deep into the fracture, finally leading to breakthrough when the longest one reaches the outlet. Some illustrations of inhomogeneous dissolution in natural fractures are compiled in Figure 1. A striking example of nonuniform dissolution is the process of limestone cave formation. Even though cave formation starts along fractures and bedding planes, which have quasi two-dimensional slot-like geometries, the mature cave is almost always a system of pipe-like conduits [*Groves and Howard*, 1994b; *Howard and Groves*, 1995], such as the one depicted in Figure 1e.

In this paper we investigate the extent to which the dissolution patterns in a fracture are controlled by distinctive features of the initial aperture distribution and to what extent they arise from random perturbations through an instability mechanism. Wormholes have also been observed in melt flows [*Aharonov et al.*, 1995; *Spiegelman et al.*, 2001] as well as in the hypogene karst [*Andre and Rajaram*, 2005; *Chaudhuri et al.*, 2008]. However, the physical mechanism behind their formation is somewhat different. The dissolution in these systems is driven by macroscopic solubility gradients, which lead to the formation of extended conduit systems, with a well-defined spacing between the wormholes. Since the wormholes form simultaneously along the entire length of the system, the competition between them is suppressed and they do not form a hierarchical, self-affine structure as is the case with the flow-driven systems.

The paper is divided as follows: in section 2 we present details of the simulation method, which follows the pioneering work reported by *Hanna and Rajaram* [1998] and *Cheung and Rajaram* [2002], but extended to much larger systems (up to 67 million cells) in order to accommodate a wide range of length scales. Results are presented in section 3 followed by a discussion of their geophysical implications in section 4 and the conclusions in section 5.

2. Simulation Method

The analysis in this paper is based on numerical simulations of the time-dependent aperture field of a dissolving fracture, using a variety of initial aperture distributions. The key assumptions are that the velocity and concentration fields can be averaged over the fracture aperture [*Hanna and Rajaram*, 1998], which allows us to study much larger systems than would be feasible with a fully three-dimensional simulation. By using parallel computing, we were able to simulate systems up to 8192 cells on a side, which for a typical grid resolution (∼1 cm) corresponds to fracture dimensions of the order of 100 m.
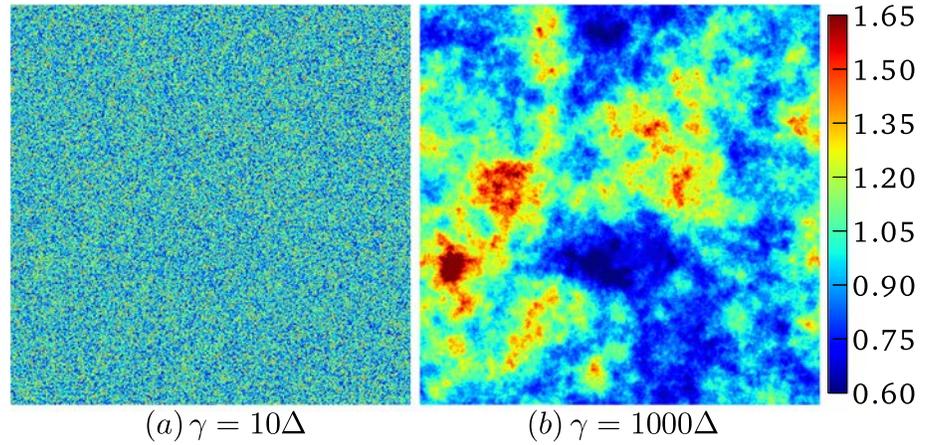
Figure 3. Initial aperture distributions in a $8192\Delta \times 8192\Delta$ fracture with roughness $\sigma = 0.2$: (a) correlation length $\gamma = 10\Delta$ and (b) correlation length $\gamma = 1000\Delta$. The color bar indicates the local variation in aperture $h(x, y)$, in units of the initial mean aperture h_0.

2.1. Fracture Geometry

The fracture geometry used in these simulations is sketched in Figure 2; here $h(x, y, t)$ is the (nonuniform) aperture, while $L \gg h$ and $W \gg h$ are the fracture dimensions. We will assume that the imposed pressure gradient is along the length of the fracture (x direction). The initial state of the system is created from a random aperture field $h(x, y, t = 0)$, with a mean aperture

$$h_0 = \langle h(t = 0) \rangle \tag{1}$$

and roughness

$$\sigma = \frac{\sqrt{\langle h^2 \rangle - \langle h \rangle^2}}{\langle h \rangle}. \tag{2}$$

We used a regular grid of points with periodic boundary conditions in the y direction and a spacing Δ between the nearest neighbor points. The aperture at each grid point was sampled from a lognormal distribution,

$$\ln h(x, y) = b + f(x, y), \tag{3}$$

with a spatial correlation length, γ, defined by the autocorrelation of the variations in f,

$$\langle f(x, y) f(x + \delta x, y + \delta y) \rangle = v^2 \exp \left[-\frac{\sqrt{\delta x^2 + \delta y^2}}{\gamma} \right]. \tag{4}$$

Initial aperture distributions with the desired mean, $h_0 = \exp(b + v^2/2)$, roughness $\sigma = \sqrt{\exp(v^2 - 1)}$, and correlation length γ, were generated using the Fourier filtering method [*Saupe*, 1988]. Two example aperture distributions, with correlation lengths of 10Δ and 1000Δ are shown in Figure 3. The large sample size ($8192\Delta \times 8192\Delta$) allows for a wide range of correlation lengths (from $2\Delta \le \gamma \le 1000\Delta$), while maintaining a statistically homogeneous initial condition. Previous work [*Hanna and Rajaram*, 1998; *Cheung and Rajaram*, 2002; *Kalia and Balakotaiah*, 2009; *Maheshwari and Balakotaiah*, 2013; *Maheshwari et al.*, 2013] only considered relatively small correlation lengths ($\gamma < 30\Delta$).

2.2. Reactive Transport Model

Fracture dissolution can be described by coupled equations for flow, concentration, and fracture aperture [*Hanna and Rajaram*, 1998; *Cheung and Rajaram*, 2002]. Fluid flow is modeled within the framework of the lubrication approximation, which assumes a parabolic velocity profile across the fracture at each location in the xy plane. The fluid flux in the fracture plane, $\boldsymbol{q}(x, y) = \int_0^h \boldsymbol{v}(x, y, z) dz$ can then be found from the lubrication equations:

$$\boldsymbol{\nabla} \cdot \boldsymbol{q} = 0, \qquad \boldsymbol{q} = -\frac{h^3}{12\mu} \boldsymbol{\nabla} p, \tag{5}$$

where μ is the fluid viscosity. Transport of reactant can be described in terms of a two-dimensional velocity-averaged or "cup-mixing" concentration field [*Bird et al.*, 2001],
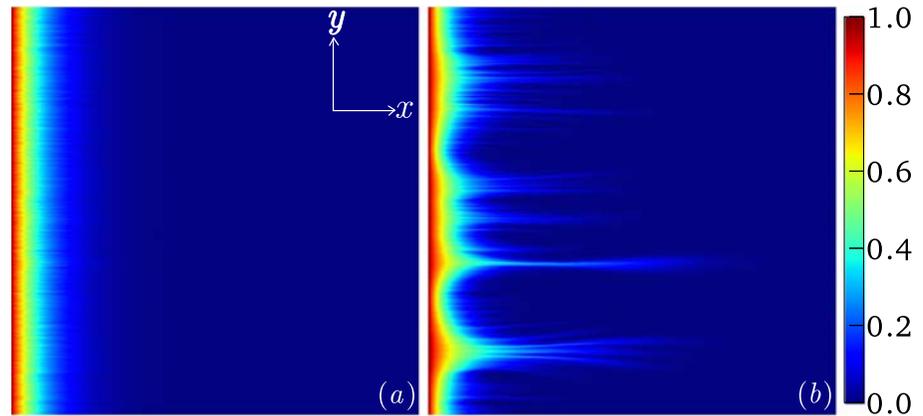
Figure 4. A dissolutional instability developing from a homogeneous initial condition in a $4096\Delta \times 4096\Delta$ fracture. The flow direction is from left to right. The panels show the dimensionless concentration field, $\hat{c}$, at (a) $t = 0$ and (b) $t = 20t_d$. The initial aperture distribution was characterized by a roughness $\sigma = 0.1$ and correlation length $\gamma = 0.014l_p$. The penetration length $l_p = 286\Delta$ was selected so that the linear stability analysis predicts exactly three wavelengths across the width of the system ($\lambda_{\max} = 4.74l_p$).

$$c(x, y) = \frac{1}{\boldsymbol{q}(x, y)} \int_0^h \boldsymbol{v}(x, y, z)c(x, y, z)\mathrm{d}z. \tag{6}$$

The three-dimensional convection-diffusion equation for reactant transport in the fracture can then be reduced to a two-dimensional convection-diffusion-reaction equation for the cup-mixing concentration [*Hanna and Rajaram*, 1998; *Detwiler and Rajaram*, 2007; *Szymczak and Ladd*, 2012],

$$\partial_t(hc) + \boldsymbol{q} \cdot \boldsymbol{\nabla}c = D\boldsymbol{\nabla}h \cdot \boldsymbol{\nabla}c - 2R(c), \tag{7}$$

where $2R(c)$ accounts for the concentration depletion at both fracture surfaces by dissolution. The dissolution reactions also increase the aperture,

$$c_{\text{sol}}\partial_t h = 2R(c), \tag{8}$$

where c_{sol} is the molar concentration of mineral. We assume the rock is composed of entirely soluble mineral, for example, calcite or gypsum.

Dissolution kinetics in fractures are often nonlinear in the concentration and limited by transport across the fracture aperture. Here we have chosen to ignore these complications and use a linear rate law, $R = k(c_{\text{sat}} - c)$, where c_{sat} is the saturation concentration of dissolved mineral ions and k is the reaction rate constant. Although kinetic order is important in one-dimensional models of fracture dissolution [*Dreybrodt*, 1990; *Groves and Howard*, 1994a; *Dreybrodt*, 1996], two-dimensional simulations [*Szymczak and Ladd*, 2011a] suggest that it may play only a minor role in actively developing wormholes. This is because the large flow in the wormhole keeps the concentration near the tip well below saturation (see section 3.3 for further discussion).

There are a number of parameters that determine the outcome of a simulation, as well as different possibilities from statistically equivalent distributions of the initial aperture. In addition to the parameters characterizing the aperture distribution—h_0, σ, and γ—there are parameters that determine the flow, transport, and reaction rate in the fracture—∇p, D, and k. The parameter space can be reduced by a suitable scaling of the fields:

$$\hat{\boldsymbol{q}} = \frac{\boldsymbol{q}}{q_0}, \quad \hat{p} = \frac{p}{l_p p_0'}, \quad \hat{c} = \frac{c_{\text{sat}} - c}{c_{\text{sat}}}, \quad \hat{h} = \frac{h}{h_0}. \tag{9}$$

Here q_0 is the flow rate in a uniform fracture of aperture h_0 with a pressure gradient p_0'; i.e., $q_0 = -h_0^3 p_0'/12\mu$. The length scale l_p is the reactant penetration length, which for convection-dominated flows (typical in fractures) is [*Szymczak and Ladd*, 2011a]

$$l_p = \frac{q_0}{2k}. \tag{10}$$

(a) $\gamma = 0.014l_p$ (b) $\gamma = 0.028l_p$ (c) $\gamma = 0.056l_p$ (d) $\gamma = 0.14l_p$
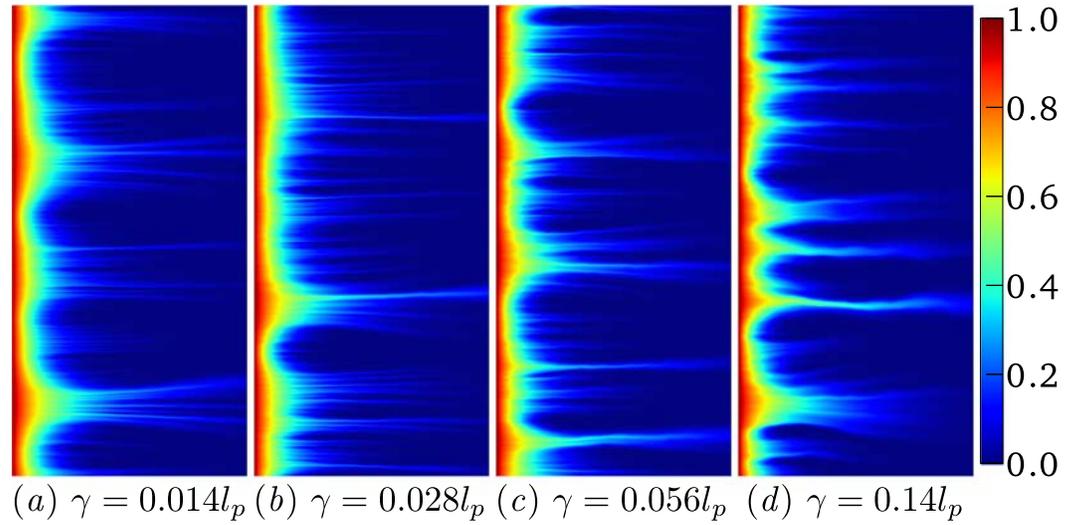
Figure 5. Concentration fields ($\hat{c}$) for different correlation lengths γ, with constant roughness $\sigma = 0.1$. The fracture dimensions and flow conditions are the same as in Figure 4. Only the inlet (left) side of the systems is shown here; the concentration in the remainder of the system is negligible. The time for each concentration profile was selected at a roughly comparable point in the evolution of the dissolution pattern: (a) $20t_d$, (b) $15t_d$, (c) $11t_d$, and (d) $7t_d$.

After scaling distances by the penetration length, $\hat{x} = x/l_p$, the flow in the fracture is described by the dimensionless equations:

$$\hat{\mathbf{\nabla}} \cdot \hat{\boldsymbol{q}} = 0, \quad \hat{\boldsymbol{q}} = \hat{h}^3\hat{\mathbf{\nabla}}\hat{p}. \tag{11}$$

At the fracture inlet $R = kc_{\text{sat}}$, and the aperture grows linearly in time with a velocity $2k\gamma$, where $\gamma = c_{\text{sat}}/c_{\text{sol}}$ is the acid capacity number (or volume of rock dissolved by a unit volume of reactant). In most geological systems $\gamma \ll 1$, for example, in calcite fractures it is of the order 10^{-4}. A natural timescale is then

$$t_d = \frac{h_0}{2k\gamma} = \frac{\tau}{\gamma}, \tag{12}$$

which is the time for the initial aperture at the inlet to double. With this scaling of length and time ($\hat{t} = t/t_d$), the dimensionless transport equation is

$$\gamma\partial_{\hat{t}}(\hat{h}\hat{c}) + \hat{\boldsymbol{q}} \cdot \hat{\mathbf{\nabla}}\hat{c} = H\hat{\mathbf{\nabla}}\hat{h} \cdot \hat{\mathbf{\nabla}}\hat{c} - \hat{c}, \tag{13}$$

where $H = 2kh_0D/q_0^2$ is a dimensionless number that determines the relative magnitudes of diffusive and convective fluxes on the scale of l_p [*Szymczak and Ladd*, 2012]. However, since $\gamma \ll 1$, we solve for the steady state concentration field directly, ignoring the time derivative in (13).

In fracture flows it is almost invariably the case that $H \ll 1$ (see section 3.3); the essential transport process is the balance between the convective flux of reactant into the fracture and the dissolution flux at the surfaces. The outcomes are then independent of H, although the simulations maintain a small diffusive current ($H \sim 10^{-6}$) to ensure stability. Note that in dissolving porous media, the opposite limit frequently applies; $H \gg 1$ and the dissolution is then independent of reaction rate [*Ortoleva et al.*, 1987; *Szymczak and Ladd*, 2013].

The dimensionless equation for the aperture increase is

$$\partial_{\hat{t}}\hat{h} = \hat{c}, \tag{14}$$

where the dimensionless aperture at the inlet, $\hat{h}(\hat{x} = 0, \hat{y})$, increases by 1 in every unit of time (the dimensionless concentration at the inlet $\hat{c}(\hat{x} = 0, \hat{y}) = 1$). Under the assumptions of linear, reaction-limited kinetics, fracture dissolution (with $H \approx 0$) is specified (in the statistical sense) by just the roughness and correlation length (in units of l_p); the mean aperture does not appear in the scaled equations.
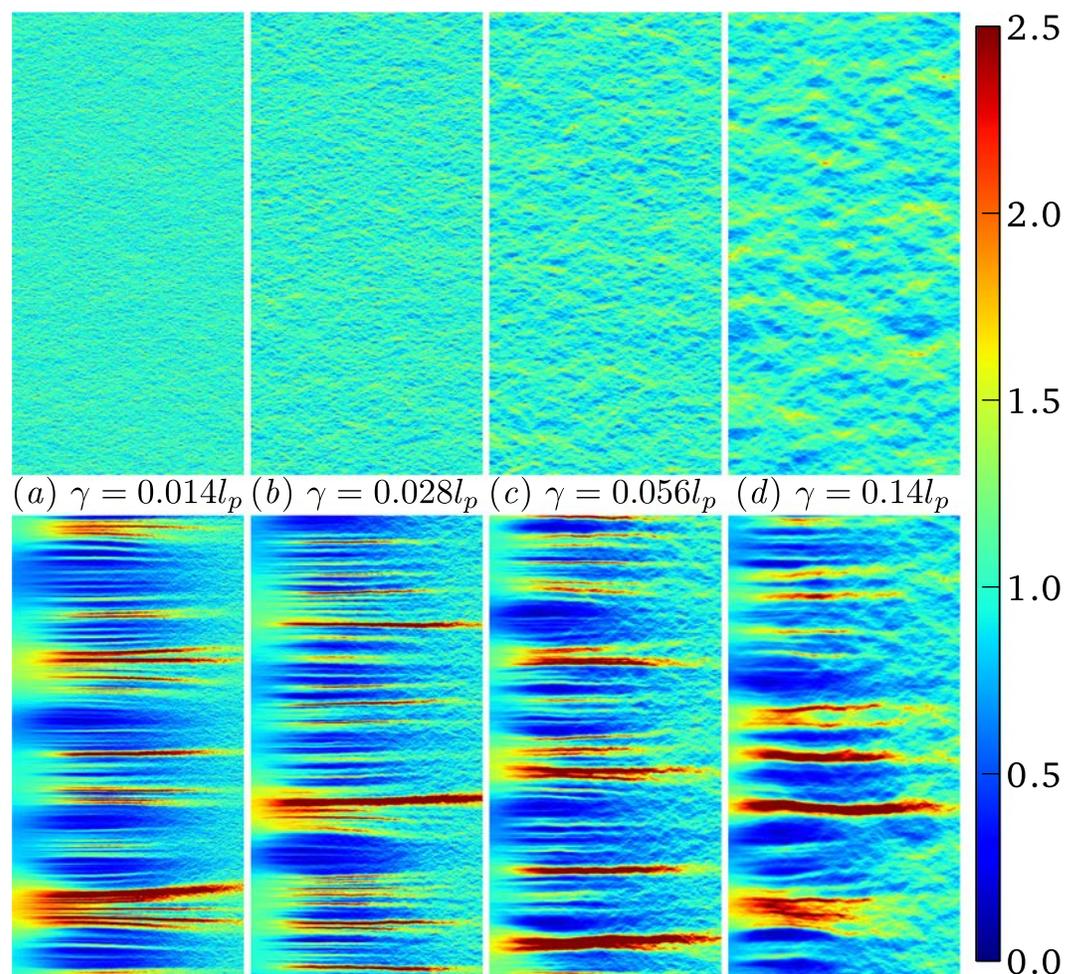
Figure 6. Root-mean-square (RMS) flow rate, $\hat{q} = \sqrt{q_x^2 + q_y^2}/q_0$, for different correlation lengths and constant roughness $\sigma = 0.1$. RMS flow rates are shown at the same elapsed times as the concentration fields in Figure 5: (a) $20t_d$, (b) $15t_d$, (c) $11t_d$, and (d) $7t_d$. Only the inlet (left) half of the system is shown in each case.

2.3. Numerical Implementation

Numerical solutions of the dimensionless equations (11), (13), and (14) were obtained from finite difference discretization. The fracture surface is divided into a structured grid with a uniform spacing, Δ, in both x and y directions. Since the fields develop in complex and unpredictable ways there is little to be gained from a graded mesh; we did not investigate the complexities associated with adaptive mesh resolution. The aperture, pressure, and concentration fields are determined at the grid positions, while the fluid flux was calculated by differencing the pressure. Upwind differencing was used to calculate the convective concentration flux throughout the domain. We found that satisfactory resolution of the concentration (the most rapidly varying field) can be obtained with 10 points spanning the penetration length l_p. In some cases we used significantly more points to increase the resolution of the images, but the dissolution patterns and flow rates were similar. An explicit time stepping method (fourth-order Runga-Kutta) was used to update the aperture fields.

The simulations employed periodic boundary conditions in the transverse (y) direction, and a constant pressure was applied at the inlet and outlet. Except for the results presented in Figure 8, the simulations were halted long before breakthrough and there was little difference in the dissolution patterns between constant flow rate and constant pressure drop conditions. A uniform concentration $\hat{c} = 1$ was set at the inlet.

In order to examine pattern formation over as wide a range of scales as possible, the equations were solved in parallel using up to 64 processors. Communication between processors was managed by the Message Passing Interface toolkit [*Forum*, 1994]. The linear systems of equations resulting from discretizing equations (11)
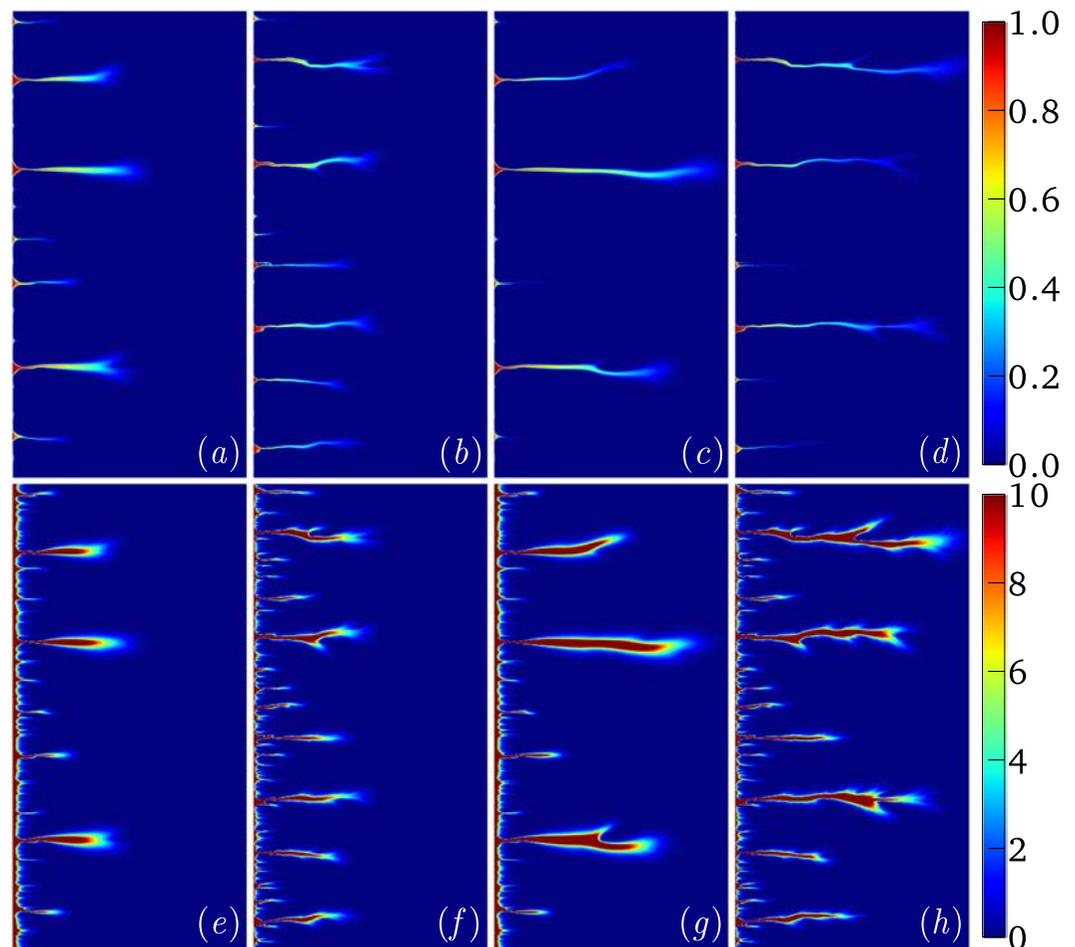
Figure 7. (a–d) Concentration distribution and (e–h) aperture growth in fractures (4096Δ × 4096Δ) of different roughness; the correlation length $\gamma = 1.4l_p$. Concentration fields $\hat{c}$ at two different times are shown in Figures 7a–7d, and the corresponding aperture growths $\delta\hat{h}$ (15) are shown in Figures 7e–7h. The odd panels (Figures 7a, 7c, 7e, and 7g) correspond to a smooth fracture, $\sigma = 0.02$, while the even panels (Figures 7b, 7d, 7f, and 7h) are for a rougher fracture $\sigma = 0.2$. (a) $\sigma = 0.02$, $t = 60t_d$; (b) $\sigma = 0.2$, $t = 60t_d$; (c) $\sigma = 0.02$, $t = 120t_d$; (d) $\sigma = 0.2$, $t = 160t_d$; (e) $\sigma = 0.02$, $t = 60t_d$; (f) $\sigma = 0.2$, $t = 60t_d$; (g) $\sigma = 0.02$, $t = 120t_d$; and (h) $\sigma = 0.2$, $t = 160t_d$. The penetration length, $l_p = 28.6\Delta$, corresponds to 30 wavelengths across the initial fracture. The complete evolution of the concentration and aperture fields are shown in Movies S1–S4 in the supporting information: Figures 7a and 7c are included in Movie S1, Figures 7b and 7d in Movie S2, Figures 7e and 7g in Movie S3, and Figures 7f and 7h in Movie S4.

and (13) were solved using the HYPRE (High Performance Preconditioners) Library [*Falgout and Yang*, 2002]. HYPRE is an open source library with a selection of solvers, preconditioners, and grid layouts, designed to solve massive, sparse linear systems of equations in parallel; we used the Semi-Coarsening Multigrid solver for these simulations.

The results in Figure 10 required an algorithm to count the number of wormholes as a function of their length. First, a threshold criterion was implemented where wormholes were defined as regions where the local aperture field was more than twice the initial mean aperture $h \geq 2h_0$. The points marking the transition between matrix and wormholes were mapped to a single contour outlining the wormholes. A distance into the fracture of the order of the penetration length ($x_0 = 4l_p$) was used to define the base of the wormholes; only those wormholes that extended beyond x_0 were counted. Wormholes were then identified by counting the crossings of the boundary contour with the line $x = x_0$. Counting at the base ensures that wormholes with multiple branches were only counted once. Finally, at any given distance $x > x_0$, a wormhole whose length was greater than or equal to x was counted, which gives rise to the distribution of channel lengths $N(L)$ in Figure 10.
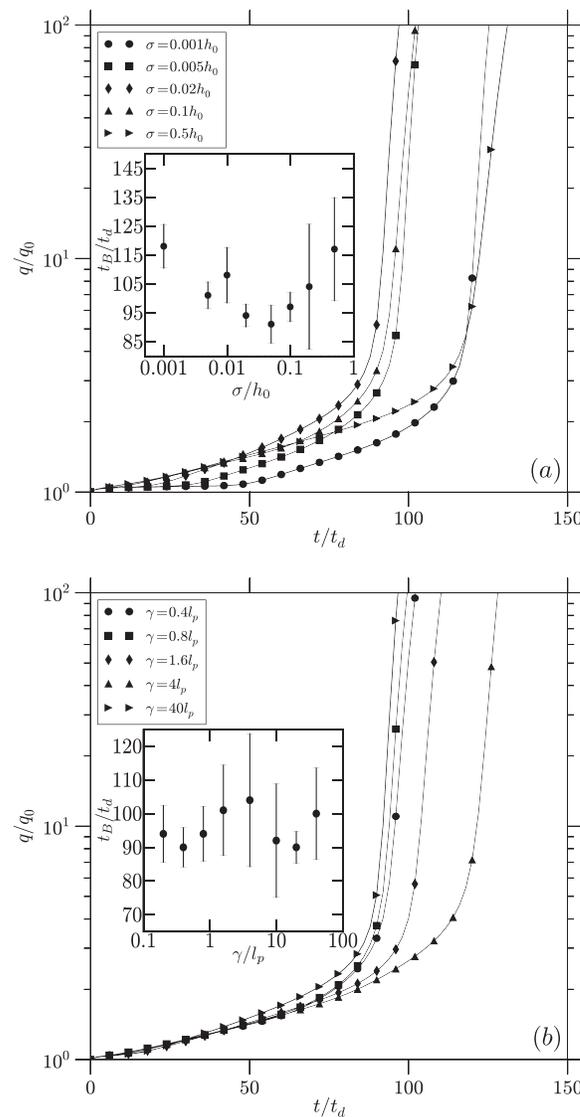
Figure 8. Flow rates in dissolving fractures: (a) varying roughness and constant correlation length ($\gamma = 4l_p$) and (b) varying correlation length and constant roughness ($\sigma = 0.2$). Sample flow rates for particular realizations are plotted up to the breakthrough times, which are characterized by a rapid increase in q. The inset figures show the average breakthrough time t_B, defined by $q(t_B) = 10q_0$, for five realizations of each initial condition; the error bars are one standard deviation. The fracture has dimensions $1024\Delta \times 1024\Delta$ with a penetration length $l_p = 10\Delta$.

3. Results

Simulations of fracture dissolution from a wide range of initial conditions have been carried out using the model described in section 2. Since this work is directed toward field-scale observations, where system boundaries do not play a significant role, l_p is the only physically important length in the system. We have investigated the dependence of the dissolution patterns on the roughness σ and correlation length γ of the initial aperture distribution. As noted in section 2, once the reactant penetration length $l_p = q_0/2k$ is fixed, the transport processes in the fracture are determined. Since lengths are scaled by l_p, the only parameters to be varied are σ and γ/l_p.

3.1. Development of Dissolution Fronts in Rough Fractures

Initially, the dissolution front is planar, as shown in Figure 4a. The concentration is constant across the fracture (y direction) with small lateral fluctuations arising from the stochastic variation in aperture. However, even a uniform aperture distribution is unstable to infinitesimal perturbations, with a characteristic wavelength proportional to the penetration length l_p. In a smooth fracture, characterized by high Péclet number transport, the most unstable wavelength is $\lambda_{\max} = 4.74l_p$ [*Szymczak and Ladd*, 2011a, 2012]. This wavelength grows exponentially faster than all the others, and a planar dissolution front develops sinusoidal perturbations [*Szymczak and Ladd*, 2011a], the remnants of which can be seen in Figure 4b in the region near the inlet. The wavelength of the high-concentration region (red and yellow) matches closely with the prediction of a Linear Stability Analysis (LSA), $\lambda_{\max} = 4.74l_p$ [*Szymczak and Ladd*, 2012]. However, as the amplitude of the perturbations grow, nonlinear couplings between the neighboring peaks cause competition for the flow [*Szymczak and Ladd*, 2009a], which leads to the development of distinct wormholes, such as those visible in Figure 4b.

The fine structure superimposed on the main flow paths arises from the fluctuations in initial aperture; it gradually vanishes as the wormholes develop further (see Figure 7 for later times). Although the specific location of individual wormholes is unpredictable, the overall characteristics of the dissolution pattern, and in particular the length and spacing of the wormholes as a function of time, are quite reproducible. In the remainder of this section we investigate the effects of initial conditions on the development of the dissolution patterns within a fracture.

Independent initial conditions were sampled from a lognormal distribution, varying the correlation length (γ) and roughness (σ). The extremes of correlation length in initial aperture fields for a roughness $\sigma = 0.2$

Figure 9. Dimensionless aperture fields ($\hat{h} = h/h_0$) in rough fractures ($\sigma = 0.2$). Results for varying correlation lengths in the initial aperture are shown at a time $t = 2000t_d$: (a) $\gamma = 0.2l_p$, (b) $\gamma = 2l_p$, (c) $\gamma = 20l_p$, and (d) $\gamma = 100l_p$. The initial aperture field is also shown and appears as a background to the developing wormholes, which appear in red. The penetration length $l_p = 10\Delta$, and the fracture dimensions were $8192\Delta \times 8192\Delta$. The aperture field at the inlet, $\hat{h}(x = 0) = 2000$, greatly exceeds the scale used in Figure 5.

are illustrated in Figure 3. Small correlation lengths lead to a uniform distribution of aperture variations over the fracture (Figure 3a), in contrast with larger γ, which has regions of highly correlated apertures (Figure 3b). The development of the concentration fields for a range of correlation lengths is shown in Figure 5. The fields were sampled when the leading wormhole reached the halfway point; the elapsed time for each snapshot is given in the caption in Figure 5. More correlated roughness promotes instability in the front, so that at higher correlation lengths patterns develop more rapidly. For $\gamma < 0.05l_p$ the concentration field shows three distinct waves, but for larger correlation lengths additional perturbations are observed, which derive from the highly correlated roughness. However, like the fine structure in Figure 4 these additional wormholes gradually die away as dissolution progresses, so that the number of wormholes at later times is roughly independent of γ (Figure 7).

The RMS flow rates $q = \sqrt{q_x^2 + q_y^2}$ in the initial fractures, shown in Figure 6 (top row), give little hint of the emerging dissolution patterns. For small correlation lengths ($\gamma < 0.05l_p$) there are no discernible flow paths in the initial fracture; the fluid flow is uniform throughout, with small random fluctuations. Nevertheless, distinct and highly correlated flow paths emerge at later times as shown in Figure 6 (bottom row). These flow paths correlate with the development of wormholes with localized concentration fields (Figure 5). The beginnings of potential flow paths can be seen at the higher correlation lengths, especially when $\gamma = 0.14l_p$. These initial flow paths appear correlated with the later development of wormholes, suggesting that highly correlated fluctuations in the initial aperture field are capable of nucleating wormholes. Interestingly the spacing between the flow paths is roughly independent of γ, although the wormholes nucleate faster in fractures with larger correlation lengths (Figure 5).

The results presented in Figures 5 and 6 show that roughness in the aperture field, especially if it is correlated over significant distances, increases the number of wormholes forming when a planar front breaks up. However, as the dissolution front develops, only a small fraction of the wormholes continue to grow, with the longer wormholes draining flow and reactant from the shorter ones. The pressure in a short wormhole is higher than the pressure in a longer neighboring wormhole because the flow rate is smaller and therefore the pressure gradient is less [*Szymczak and Ladd*, 2006]. Long wormholes thereby capture fluid and reactant from surrounding regions, and their growth is reinforced at the expense of neighboring wormholes. Thus, the pattern coarsens as dissolution proceeds, with an ever increasing distance between the wormholes.

Concentration ($\hat{c}$) and aperture growth,

$$\delta\hat{h}(x, y, t) = \hat{h}(x, y, t) - \hat{h}(x, y, 0), \qquad (15)$$
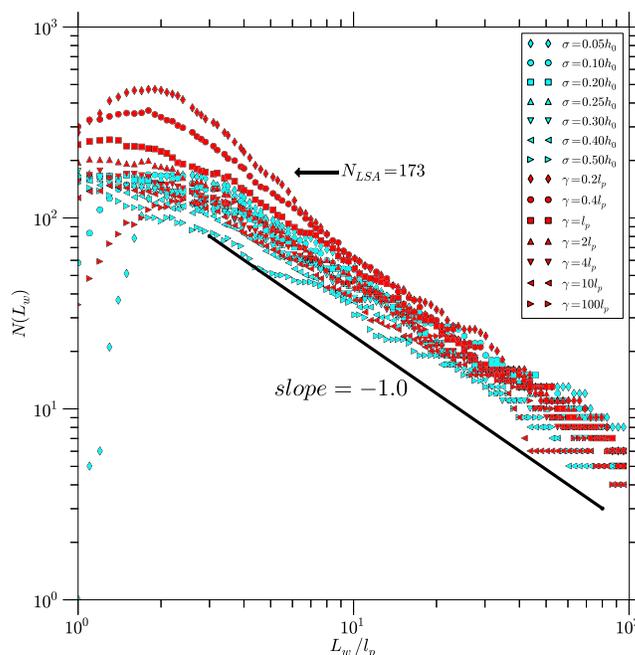
Figure 10. Distribution of wormhole lengths in rough fractures. The number of wormholes across the width of the system is shown as a function of the wormhole length for different roughness and constant correlation length ($\gamma = 4l_p$) and for different correlation lengths with constant roughness ($\sigma = 0.2$). The horizontal arrow indicates the number of wavelengths predicted by linear stability analysis, $N_{\text{LSA}} = 173$. The penetration length $l_p = 10\Delta$, and the fracture dimensions were $8192\Delta \times 8192\Delta$.

provide different ways to examine fracture dissolution patterns. Concentration fields (for example, Figures 7a–7d) only show the active wormholes; once a wormhole stops growing, its concentration is depleted and transferred to the active flow paths. But the aperture distribution preserves the whole history of the dissolution, including those regions which are no longer growing. It is these morphological changes that can be observed in the field. Figure 7 shows concentration fields and aperture growth for larger fractures than in Figures 5 and 6. At later times ($t > 100t_d$) the number of active wormholes is nearly independent of roughness; compare the concentration profiles in Figures 7c and 7d. An approximate doubling of the wormhole length — Figure 7a→Figure 7c or Figure 7b→Figure 7d — results in half as many active wormholes. By contrast the aperture growth shows that there were more channels at earlier times in the rougher fracture — Figures 7f and 7g — than in the smoother fracture — Figures 7e and 7f.

The increased roughness — Figures 7b, 7d, 7f, and 7g — causes frequent attempts at branching, but the side branches are quickly killed off as the longer wormhole drains their flow [*Cheung and Rajaram*, 2002]. Thus, the number of active wormholes remains independent of roughness, but the velocity of the tips is reduced by repeated attempts at branching. Wormholes in rougher fractures — Figures 7d and 7h — propagate more slowly than wormholes in smooth fractures — Figures 7c and 7g. Nevertheless, the dissolution patterns at later times are strikingly similar, ruled by wormhole competition which sets the scale for the distance between the wormholes. The competition between developing wormholes can be seen in Movies S1–S4; the connection of each movie to the panels in Figure 7 is indicated in the caption.

3.2. Breakthrough and the Distribution of Wormhole Lengths
The evolution of the volumetric flow rate is shown in Figure 8 for a range of initial aperture distributions: from $\sigma = 0.001$ to $\sigma = 0.5$ and from $\gamma = 0.4l_p$ to $\gamma = 40l_p$. A small penetration length, $l_p = 10\Delta$, was chosen to increase the number of flow paths and hence the competition between the growing wormholes.

The initiation of localized flow paths (or wormholes) plays a critical role in the evolution of fracture aperture, reducing the breakthrough time by orders of magnitude in comparison with a smooth (one-dimensional) fracture [*Szymczak and Ladd*, 2011a]. With linear reaction kinetics (7) the length of a uniform aperture increases only logarithmically in time, and the smoothest fractures in Figure 8 ($\sigma = 0.001 - 0.005$) follow this trend
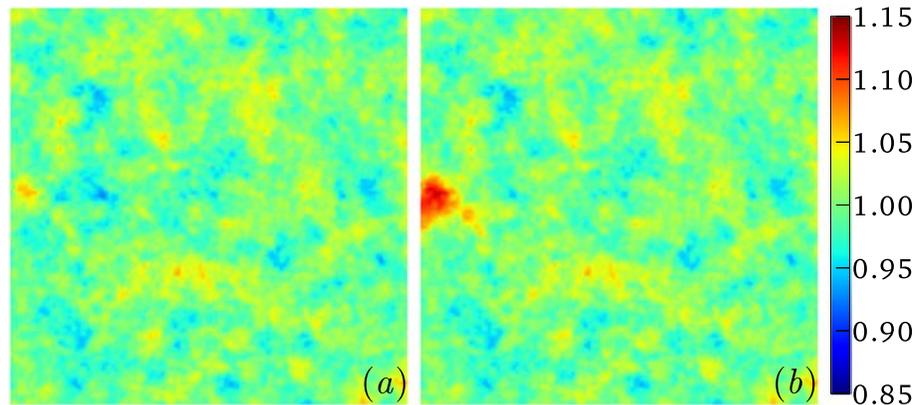
Figure 11. Aperture distribution in a fracture seeded with a local perturbation at the inlet (18): (a) background lognormal distribution with roughness $\sigma = 0.05$ and correlation length $\gamma = 4\Delta$ and (b) same distribution with the seed superimposed. The image shows a $128\Delta \times 128\Delta$ portion of a $2048\Delta \times 2048\Delta$ fracture, located at the inlet.

initially. There is essentially no increase in flow rate for times up to $20–50 \, t_d$; but after wormholes start to form the flow rate increases more rapidly.

Breakthrough times, t_B, exhibit a nonmonotonic dependence on roughness (Figure 8a, inset), which reflects the interplay between the onset of the instability and the growth of individual wormholes. Higher roughness promotes the onset of instability, and an initially flat dissolution front develops wormholes faster in rougher fractures. However, roughness impedes the extension of these wormholes because of the tendency to form side branches. There is a minimum in the breakthrough time, which in these simulations ($2048\Delta \times 2048\Delta$) occur around a roughness, $\sigma \approx 0.05$. These relatively smooth fractures have sufficient variation in permeability to break the front quickly, but not sufficient to cause extensive branching. The canceling effects of roughness—more rapid initiation of wormholes but slower propagation—means that breakthrough times show little variation with aperture distribution, staying within the range $90t_d–120t_d$, over 2 orders of magnitude variation in roughness and correlation length.

A similar dependence of the breakthrough times on roughness has been reported for dissolving fractures [*Hanna and Rajaram*, 1998; *Cheung and Rajaram*, 2002] and porous media [*Kalia and Balakotaiah*, 2009; *Maheshwari and Balakotaiah*, 2013; *Maheshwari et al.*, 2013]. Interestingly, some of these features turn out to be scale dependent, with smaller systems showing nonergodic behavior, with a large variability in breakthrough times between different realizations of the same aperture distribution. For example, in a small (12.5 m × 12.5 m) fracture, *Hanna and Rajaram* [1998] find t_B to be monotonically decreasing with σ, whereas *Cheung and Rajaram* [2002] find that larger systems show a minimum in t_B associated with the mechanism elucidated above. Nevertheless, for large enough σ, *Cheung and Rajaram* [2002] find that t_B again decreases, due to the strong flow focusing of the rough fracture, which results in the rapid formation of a solitary wormhole. Our data, obtained for even larger fractures, suggest that this is another finite size effect. Thus, in the limit of an infinite domain we expect a single minimum in $t_B(\sigma)$, a result of the interplay between flow focusing and branching at the channel tips. A pronounced minimum in $t_B(\sigma)$ was also found in porous media [*Kalia and Balakotaiah*, 2009; *Maheshwari and Balakotaiah*, 2013; *Maheshwari et al.*, 2013], both two and three dimensions.

The breakthrough time shows no systematic dependence on correlation length, at least at the level of statistical accuracy achieved in these simulations (10%). There is more statistical variability at intermediate correlation lengths, as measured by the larger variance, than at either extreme. By contrast, a minimum in $t_B(\gamma)$ was found in simulations of porous media dissolution [*Kalia and Balakotaiah*, 2009; *Maheshwari and Balakotaiah*, 2013; *Maheshwari et al.*, 2013]. It is not clear if this is a consequence of the smaller system sizes used in that work or an intrinsic difference between fractures and porous media.

In order to investigate flow focusing over as wide a range of length scales as possible, we have simulated a number of systems on a domain of 8192 × 8192 cells, varying both the roughness and correlation length. Images of the aperture fields at late times ($t = 2000t_d$) are shown in Figure 9 for a range of correlation lengths. The range of apertures is too large to be rendered (the maximum aperture in these simulations is $2000h_0$),
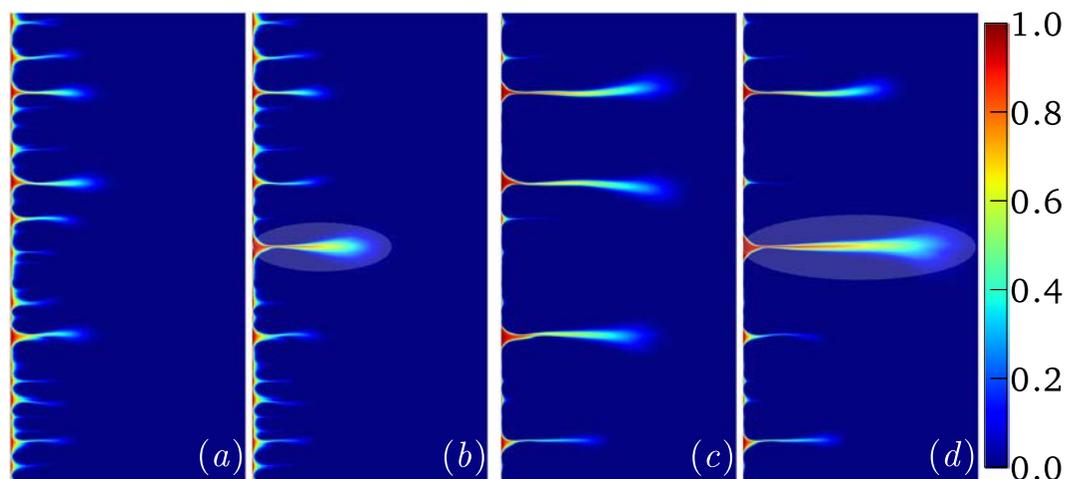
Figure 12. Comparison of concentration fields in a seeded and unseeded fracture. A localized increase in aperture (18) is superposed on a random distribution with roughness $\sigma = 0.05$ and a correlation length $\gamma = 0.166 l_p$. The fracture dimensions are $2048\Delta \times 2048\Delta$. The panels compare the concentration fields at two different times: (a) $t = 25 t_d$ unseeded, (b) $t = 25 t_d$ seeded, (c) $t = 50 t_d$ unseeded, and (d) $t = 50 t_d$ seeded. The channel growing from the initial seed is shown with a semitransparent overlay. The penetration length, $l_p = 24\Delta$.

and the scale must be truncated (at $5h_0$); the wormholes then appear as dark red regions. The initial aperture distribution is also shown and appears as a background image to the well-defined wormholes.

Late time dissolution patterns ($t = 2000 t_d$) are shown in Figure 9 for four different correlation lengths: $\gamma = 0.2 l_p$, $\gamma = 2 l_p$, $\gamma = 20 l_p$, and $\gamma = 100 l_p$. The dissolution patterns show constant attempts at branching as the wormholes propagate, which is characteristic of a rough fracture [*Cheung and Rajaram*, 2002]. However, the newly formed branches are suppressed by competition with the parent wormhole, and on large scales the wormholes tend to grow more or less straight, parallel to the pressure gradient (left to right). However, as the correlation length increases, the initial aperture distribution starts to influence the growth of the wormholes. In Figures 9c and 9d it can be seen that wormholes are at least partly following initial regions of large aperture. Nevertheless, because the flow paths are controlled by the length of the longest wormholes, the same selection mechanism operates irrespective of correlation length. Thus, the number of channels of a given length is approximately independent of correlation length. The velocity of the wormholes is insensitive to the correlation length of the initial aperture, varying by about 50% over the range of γ we investigated.

The concentration fields in Figure 7 indicate the active (or growing) wormholes, whereas the count $N(L_w)$ in Figure 10 includes all wormholes with length greater than L_w, both active (still growing) and inactive (no longer growing). It has been previously noticed that a long wormhole drains reactant from the region around it up to a distance comparable to its length [*Hoefner and Fogler*, 1988; *Szymczak and Ladd*, 2009a]. The validity of this relationship can be seen in Figure 7; the spacing between the active wormholes (those regions with significant reactant concentration) is roughly the same as their length. Thus, a dissolution pattern automatically coarsens, with fewer, longer wormholes as time progresses.

Insight into the mechanisms underlying wormhole competition has been obtained from a network model [*Szymczak and Ladd*, 2006]. Wormholes were represented by a small resistance per unit length, with a much larger resistance connecting adjacent wormholes through the surrounding matrix. As long as there was a significant contrast between the wormhole and matrix permeabilities, the dissolution patterns were insensitive to the precise values of these parameters. The system was seeded with up to 1200 short wormholes which then extended according to the local current of reactive fluid through the tip. The distribution of wormhole lengths (both active and inactive) was found to be insensitive to the initial distribution of wormhole lengths, decaying as a power law in the length,

$$N(L_w) \sim L_w^{-1.25}, \tag{16}$$

over about a decade in N.

In this work we used the aperture model to perform a similar study without the limitations imposed by the network model. We used large systems ($8192\Delta \times 8192\Delta$), but still with significantly fewer wormholes than in
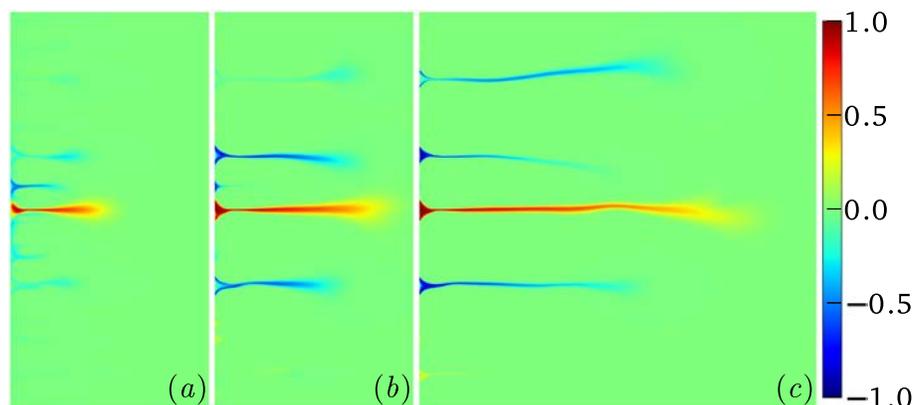
Figure 13. Difference in the (dimensionless) concentration fields between a seeded and unseeded fracture. The results illustrated in Figure 13 are replotted as a difference field, $\delta\hat{c} = \hat{c}_{seed} - \hat{c}$, at different times: (a) $t = 25t_d$, (b) $t = 50t_d$, and (c) $t = 125t_d$. The time evolution of the difference field can be seen in Movie S5.

the network model; according to LSA [*Szymczak and Ladd*, 2011a], we expect 173 waves across the width of the fracture. The simulations cover a wide range of roughness and correlation lengths (up to 1000Δ) but show a remarkably similar distribution in each case, with a peak in the number of wormholes near $L_w = l_p$ followed by a monotonic decay roughly proportional to $1/L_w$. The wormhole detection algorithm (section 2.3) requires a finite amplitude perturbation in the front in order to register; thus, the number of wormholes detected initially increases. It takes longer for the instability to develop in smoother wormholes, but the maximum number is similar to the prediction of the LSA. When the roughness in the initial fracture is large and highly correlated, wormholes form in regions of large aperture and a high degree of branching and tip splitting is seen later on (Figure 9). Nevertheless, the later dissolution is characterized by about the same number and length of wormholes regardless of the initial aperture distribution. The coarsening of the dissolution pattern follows a power law, as in the network model, but with an exponent closer to unity

$$N(L_w) \sim 1/L_w. \tag{17}$$

A similar exponent has been reported in numerical studies of wormhole growth in a network model of a two-dimensional porous matrix [*Budek and Szymczak*, 2012]. Importantly, it also agrees with theoretical results on the scaling of dendrite lengths [*Krug et al.*, 1993] in models where the dendrites grow in response to a field that satisfies the Laplace equation. In the present context, the pressure field in the undissolved rock satisfies a Laplace equation, because the aperture is nearly uniform, with $h \approx h_0$. The results of *Krug et al.* [1993] would then indicate that (up to logarithmic corrections) $N(L_w) \sim 1/L_w$ if we assume that (a) the hydraulic resistance of the wormholes is negligible in comparison with the undissolved matrix and (b) the a wormhole grows with a speed proportional to the pressure gradient at its tip.

Note that the scaling (17) implies that the characteristic separation between wormholes of length L_w, $w(L_w) = W/N(L_w)$, is proportional to L_w; the data in Figure 10 imply that the proportionality constant is in the range 1–2. In other words, the spacing between wormholes is comparable to the wormhole length. This is consistent with previous observations [*Hoefner and Fogler*, 1988; *Szymczak and Ladd*, 2009a] that the distance over which a wormhole drains the reactant from neighboring wormholes is proportional to its length. This observation suggests an interesting geological connection; fractures dissolving by the mechanisms described in this paper would develop dissolution patterns where the wormhole length and the wormhole spacing are of comparable scale.

3.3. Mapping to Geophysical Lengths and Times

In section 2.2 it was shown that in fracture dissolution (with linear kinetics) there is only a single transport parameter, the reactant penetration length $l_p = q_0/2k$; our results have been presented in terms of this length scale. To give a sense of the physical scales involved, we reevaluate the results presented in Figures 8–10 in terms of parameters consistent with dissolution of fractured carbonates. The reactant penetration length in carbonate rocks is usually less than 1 m [*White and Longyear*, 1962; *Dreybrodt*, 1990]. For example, if the initial mean aperture is 0.2 mm and the hydraulic gradient is 2%, the volume flux in the fracture

$(a)\ \sigma = 0.02h_0$ $(b)\ \sigma = 0.05h_0$ $(c)\ \sigma = 0.1h_0$ $(d)\ \sigma = 0.2h_0$
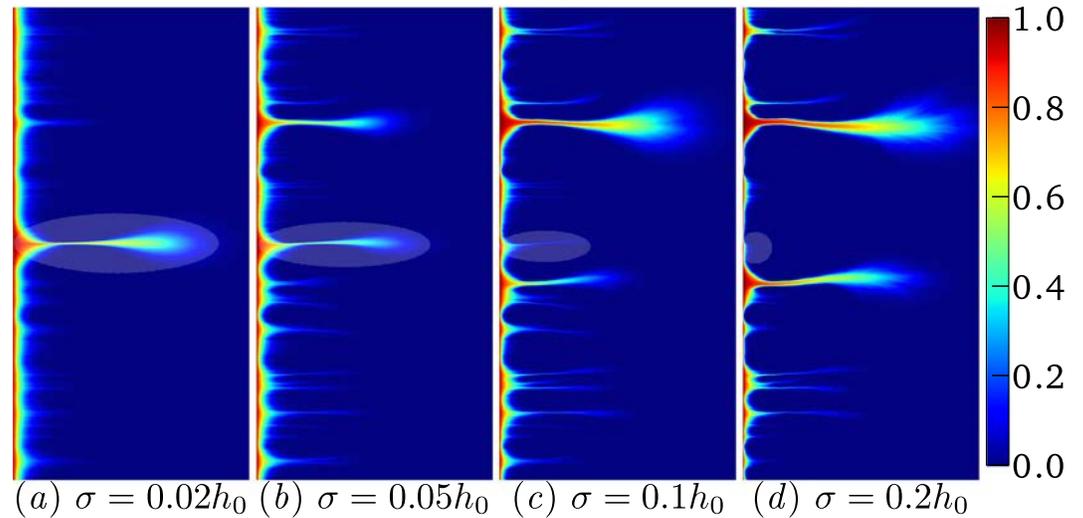
Figure 14. Concentration fields in a seeded fracture with different roughness. A localized increase in aperture (18) is superposed on random distributions with varying roughness but constant correlation length $\gamma = 0.042l_p$. The panels show the concentration field at a time $t = 24t_d$, when the wormholes are well developed but have still only grown to about one quarter of the length of the fracture: (a) $\sigma = 0.02$, (b) $\sigma = 0.05$, (c) $\sigma = 0.1$, and (d) $\sigma = 0.2$. The fracture dimensions are $8192\Delta \times 4096\Delta$, and the penetration length, $l_p = 95\Delta$, corresponds to 10 wormholes developing at early times. The seed was larger in this case ($A = 0.1$, $\alpha\Delta = 0.02$, $\beta\Delta^2 = 0.005$), more than compensating for the doubling in system width. The channel growing from the initial seed is shown with a semitransparent overlay.

$q_0 \approx 10^{-3}\,\mathrm{cm^2 s^{-1}}$; with a reaction rate constant $k = 2.5 \times 10^{-5}\,\mathrm{cm^2 s^{-1}}$ [*Dreybrodt*, 1996] the penetration length $l_p \approx 20$ cm. Since the numerical method requires about 10 cells to resolve the concentration field across a distance l_p, this sets the fracture size in Figure 8 as 40 m and as 160 m in Figures 9 and 10, with the individual grid points about 2 cm apart. The inlet doubling time t_d determined from the saturation concentration of calcium ions; taking $c_{\mathrm{sat}} = 2 \times 10^{-3}$ m [*Dreybrodt*, 1996] and $c_{\mathrm{sol}} = 27$ m we have from equation (12) $t_d \approx 0.17$ years. Thus, the breakthrough time for a carbonate fracture 40 m × 40 m is estimated to be approximately 20 years.

Nonlinear kinetics accelerates the growth of fracture aperture in a one-dimensional model [*Dreybrodt*, 1990; *Groves and Howard*, 1994a; *Dreybrodt*, 1996], but in two-dimensional models flow focusing is more important than kinetic order [*Szymczak and Ladd*, 2011a], at least when there are multiple flow paths in the fracture. As wormholes form, the high flow rates in the wormhole convect reactant much further downstream than in the surrounding matrix (Figure 7); the concentration at the tips of the wormholes remains far from saturation, minimizing the effects of nonlinear kinetics. Competition between wormholes remains the most important mechanism in determining the evolution of the flow rate in the fracture, until either the flow breaks through to the outlet or only a single wormhole remains. Nonlinear kinetics are important in high-aspect ratio fractures ($L : W \gg 1$), where competition reduces the region of significant flow to a single pathway long before breakthrough. However, in this paper we concentrate on systems where many wormholes compete for flow and therefore stay largely within the regime of linear reaction kinetics.

3.4. The Effects of Local Inhomogeneities

The heterogeneity in the permeability of fractured rocks cannot be entirely captured by stochastic variations in fracture aperture. In this section we investigate the dissolution of a fracture that is seeded with a localized increase in aperture near the center of the inlet:

$$\hat{h}_{\mathrm{seed}}(x, y) = \hat{h}(x, y) + Ae^{-\alpha x}e^{-\beta(y-W/2)^2}. \tag{18}$$

The perturbation has an amplitude $A = 0.1$ and extends over distances of the order of 10–20Δ: $\alpha\Delta = 0.05$, $\beta\Delta^2 = 0.01$. A portion ($128\Delta \times 128\Delta$) of the initial aperture field ($2048\Delta \times 2048\Delta$) is shown in Figure 11. The seeded region is larger than the correlation length ($\gamma = 4\Delta$) but much smaller than the fracture dimensions.

Concentration fields for seeded and unseeded apertures ($\hat{h}_{\mathrm{seed}}$ and $\hat{h}$) are compared in Figure 12, at times of $25t_d$ (a and b) and $50t_d$ (c and d). Results for the unseeded aperture $\hat{h}(x, y)$, where all the wormholes
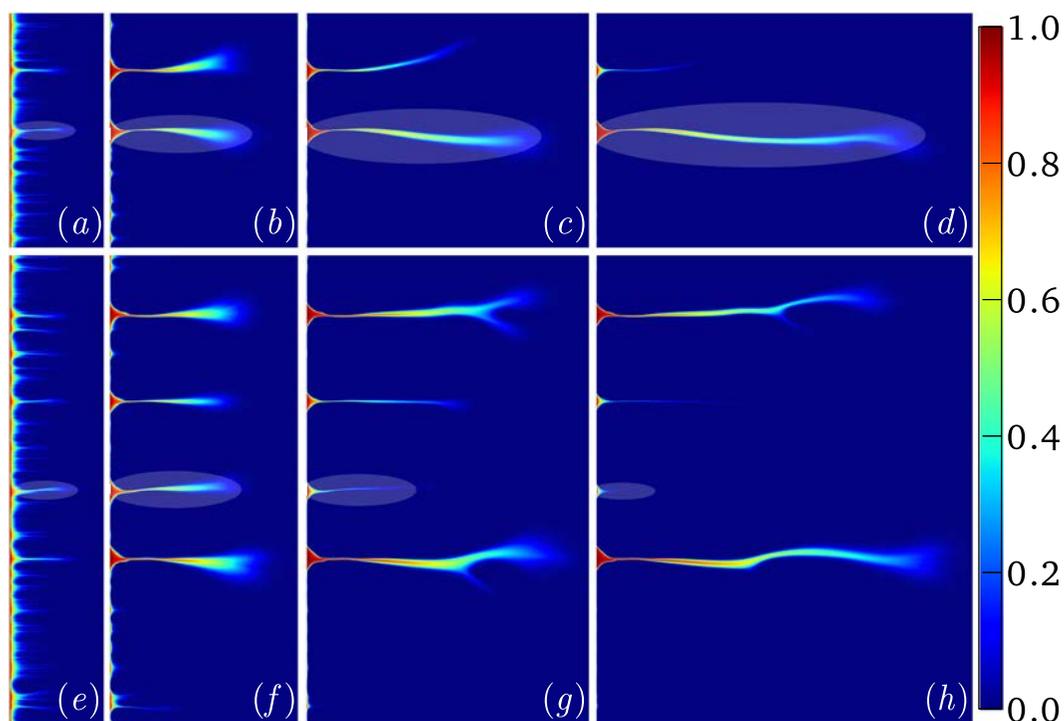
Figure 15. Concentration fields in a seeded fracture with different dimensions. A localized increase in aperture is superposed on a random distribution (parameters as in Figure 14) with fracture dimensions are (a–d) $8192\Delta \times 4096\Delta$ and (e–h) $8192\Delta \times 8192\Delta$. The panels show the concentration field at different time: (Figures 15a and 15e) $t = 20t_d$, (Figures 15b and 15f) $t = 40t_d$, (Figures 15c and 15g) $t = 80t_d$, and (Figures 15d and 15h) $t = 120t_d$. The penetration length, $l_p = 95\Delta$, corresponds to 10 wormholes (Figures 15a–15d) and 20 wormholes (Figures 15e–15h) developing at early times. The channel growing from the initial seed is shown with a semitransparent overlay.

nucleate spontaneously, are shown in Figures 12a and 12c while Figures 12b and 12d are for the seeded aperture $\hat{h}_{seed}(x, y)$, which begins with a small localized wormhole at the center. The prominence of the seeded wormhole is clearly visible in Figure 12; it is broader and grows faster than "natural" wormholes that are spontaneously nucleated. Nevertheless, its range of influence on the neighboring wormholes is still limited by its length as in Figure 7; the more distant fingers in Figures 12b and 12d are almost exact replicas of the corresponding wormholes in the unseeded fracture.

A comparison between seeded and unseeded fractures can be made more directly by plotting the difference in concentration fields,

$$\delta\hat{c}(x, y) = \hat{c}_{seed}(x, y) - \hat{c}(x, y) \tag{19}$$

between seeded ($\hat{c}_{seed}$) and unseeded ($\hat{c}$) fractures. In Figure 13 red and yellow indicate regions of large positive difference, where the seeded fracture has a wormhole and the unseeded one does not, while blue (large negative difference) indicates regions where the unseeded fracture has a wormhole and the seeded one does not.

At early times ($t = 25t_d$), the wormholes in the upper and lower quarters are growing independently of the seed (Figure 12) as can be seen by the absence of a difference field; only the region near the seed is strongly perturbed. Later ($t = 50t_d$) the wormholes within the central half of the fracture have been killed off by the seed (Figure 12d), while even the most distant wormholes are being weakened by the competition with the seeded wormhole. Finally at late times, just before breakthrough ($t = 120t_d$), the seeded wormhole has drained all the reactant from the spontaneously nucleating ones. The time evolution of the difference field, $\delta\hat{c}$, can be followed in Movie S5.

When the roughness in the aperture field is small, evolution of permeability in a seeded fracture is governed by the local perturbation, which draws all the flow due to lack of alternate flow paths (Figure 14a). This results in the local perturbation propagating without significant competition and hence overcoming the natural

Figure 16. Solution pipes in the limestone quarry at Smerdyna (Poland). Photo courtesy of dr Łukasz Użarowicz (Warsaw University of Life Sciences - SGGW, Poland). The longest wormhole in the photograph is about 5 m.

instability. However, the effects of local heterogeneity can be overwhelmed by spontaneous nucleation of flow paths. With increasing roughness, wormholes nucleate more frequently due to the larger number of these flow paths. This introduces competition with the local heterogeneity, and if the roughness is sufficiently high, the spontaneously nucleating wormholes can overwhelm the local perturbation. In Figure 14b, the seeded wormhole still manages to overcome the natural instability, despite the increased competition, although only by a small margin. Figures 15c and 15d show that with additional roughness the dominant wormhole arises from the natural inhomogeneities in the fracture rather than the local perturbation in the initial condition.

When the competition between seeded and spontaneously nucleating wormholes is comparable, as in Figure 14b, the outcome of this competition can depend on the size of the system. In Figure 15, the evolution of the relatively smooth fracture ($\sigma = 0.05$) shown in Figure 14b is compared with a system twice as wide, holding all the other parameters the same. In the 4096Δ wide fracture (Figures 15a–15d) the seeded wormhole eventually overwhelms the dominant natural wormhole (in the upper quarter of the fracture). However, in the wider 8096Δ system the reverse happens; here the spontaneous wormholes eventually overwhelm the seeded wormhole and one of the spontaneously nucleating wormholes eventually breaks through.

The number of flow paths through the fracture nucleating at any given time increases in proportion to the width of the system, as illustrated in Figure 15, thereby increasing the competition with the seed. Moreover, the seeded wormhole has to grow to longer lengths to diminish the flow in increasingly distant wormholes, which then have more chance to develop into the dominant flow path. Hence, for large enough systems, it seems plausible that the naturally growing instability will eventually overwhelms any local perturbation.

4. Geophysical Implications

Dissolution coupled with the flow has been recognized as an example of what has come to be called "self-organization" [*Ortoleva et al.*, 1987; *Spiegelman et al.*, 2001]—a small enhancement in permeability at some point in the reaction front increases the fluid flow in that region, which convects reactant further downstream. By this means any local variation in permeability is amplified as the reaction front passes through and propagates downstream with the front, eventually developing into wormholes. As we have demonstrated in this work, the statistical properties of the developing wormhole system are independent of the initial aperture distribution (Figure 10); a wide range of roughness and correlation lengths in the initial aperture gives rise to an essentially identical $1/L$ distribution of wormhole lengths. On the other hand, the positions of individual wormholes can but do not need to be influenced by local vugs or cavities, which are a characteristic feature of carbonate porosity [*Flügel*, 2004]. These features can trigger the formation of wormholes in their
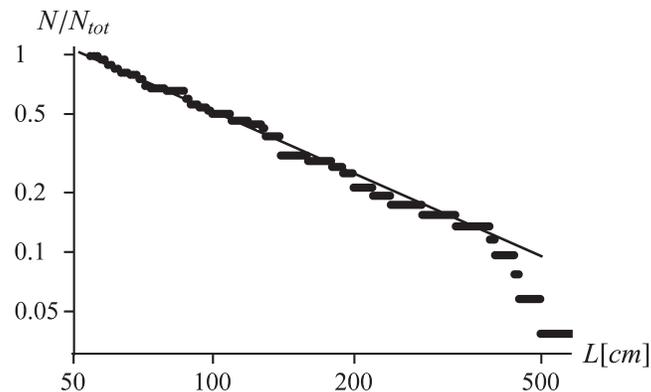
Figure 17. The cumulative distribution $N(L)$ of solution pipe lengths for the data reported in *De Waele et al.* [2011] restricted to the pipes the full length of which is uncovered. The solid line has a slope of 1.05.

vicinity, but even in this case such a wormhole can eventually lose the competition with the spontaneously appearing structures, particularly if they were formed at distances larger than the length of the initial cavity, which prevented them from being screened in the early stages of their development.

It is precisely the strong competition between wormholes that makes the effects of the initial aperture distribution less pronounced with time (for example, Figure 7). The larger flow in a wormhole leads to increased dissolution, which generates the positive feedback loop resulting in fast growth of the longer wormholes and starvation of the shorter ones. The process repeats itself, leading to the appearance of a scale-invariant distribution of wormhole lengths, wiping out all the information about the initial conditions. The hierarchical, $1/L$ distribution will then appear no matter if the initial wormholes are formed spontaneously or are triggered by preexisting vugs. Such hierarchical distributions, with many small wormholes and just a few longer ones, are indeed a characteristic feature of dissolving systems, as illustrated in Figure 16, which shows a system of solution pipes uncovered in a limestone quarry in Smerdyna, Poland.

De Waele et al. [2011] have described a collection of more than 200 solution pipes in the coastal areas of the Mediterranean, suggesting that the distribution of lengths follows an exponential law. Whereas some of the data quoted in *De Waele et al.* [2011] seem to support this hypothesis, there are two observations which suggest an alternative interpretation. First, most of the pipes measured by *De Waele et al.* [2011] have been partially buried, and thus, their full length remains unknown. Second, some of the distributions reported there have shown a characteristic break when plotted on a semilog scale and thus needed to be fitted by two independent exponential distributions, one for small L and one for large L. As shown previously [*Szymczak and Ladd*, 2009b], a double exponential distribution can in fact be a power law in disguise. With that in mind, we have plotted the length distribution reported in *De Waele et al.* [2011] on a log-log scale, restricting ourselves to fully visible pipes for which the full length can be measured. The resulting distribution, shown in Figure 17, is well fitted by a power law model with an exponent of 1.05, close to the one suggested by our studies and in agreement with the exponents reported previously for similar systems [*Krug et al.*, 1993; *Szymczak and Ladd*, 2006; *Budek and Szymczak*, 2012].

Some features of hierarchical growth manifest themselves in the examples shown in Figure 1. Figure 1a depicts the outlet of an inclined fracture located near the bottom of one of the quarry walls, transporting water from the surface about 2 m above. On the other hand, Figure 1b shows the inlet of a fracture located on the floor of the quarry, which collects water that then percolates vertically downward. The difference between the fracture inlet and output is reflected in the characteristics of the wormholes. At the inlet (Figure 1b) the distance between the wormholes is comparable to their diameter, a feature also observed in our simulations (Figure 9). On the other hand, in Figure 1a we observe the outlets of the only two wormholes that have survived the competition as they propagated along the fracture. Their separation ($\sim$1 m) is much larger than their diameter ($\sim$10 cm) and comparable with the length of the fracture ($\sim$2 m) as measured from the surface above. This agrees with our general observation that the spacing between the active wormholes should be comparable to their length.

5. Conclusions

In this paper, we have focused on the characteristics of wormholes growing in single fractures. Our conclusions are based on numerical simulations, supplemented with field observations. The results suggest that fracture dissolution patterns are largely insensitive to the initial conditions in the fracture. This has been established over a wide range of roughness and correlation lengths, which in many cases are larger than what can be expected in natural fractures. Nevertheless, at long times wormhole competition overwhelms the initial variations in aperture distribution, resulting in a universal relation between the separation of the wormholes and their length. This hierarchy of scales even persists in the presence of localized perturbations in the fracture aperture (vugs), which if the sample is large enough tend to be overwhelmed by the spontaneous growth of instabilities. A natural consequence of wormhole competition is that the separation between growing wormholes corresponds roughly to their length, something that is borne out by field observations.

References

Aharonov, E., J. Whitehead, P. Kelemen, and M. Spiegelman (1995), Channeling instability of upwelling melt in the mantle, *J. Geophys. Res.*, *100*, 433–455.

Andre, B. J., and H. Rajaram (2005), Dissolution of limestone fractures by cooling waters: Early development of hypogene karst systems, *Water Resour. Res.*, *41*(1), 1–16, doi:10.1029/2004WR003331.

Bird, R. B., W. E. Stewart, and E. N. Lightfoot (2001), *Transport Phenomena*, John Wiley, Department of Chemical Engineering, Madison, Wisconsin.

Budek, A., and P. Szymczak (2012), Network models of dissolution of porous media, *Phys. Rev. E*, *86*, 056318.

Carroll, S., Y. Hao, M. Smith, and Y. Sholokhova (2013), Development of scaling parameters to describe CO_2-rock interactions within Weyburn-Midale carbonate flow units, *Int. J. Green Gas Cont.*, *16*, S185–S193.

Chadam, D., D. Hoff, E. Merino, P. Ortoleva, and A. Sen (1986), Reactive infiltration instabilities, *J. Appl. Math.*, *36*, 207–221.

Chaudhuri, A., H. Rajaram, and H. Viswanathan (2008), Alteration of fractures by precipitation and dissolution in gradient reaction environments: Computational results and stochastic analysis, *Water Resour. Res.*, *44*, W10410, doi:10.1029/2008WR006982.

Chaudhuri, A., H. Rajaram, and H. Viswanathan (2013), Early-stage hypogene karstification in a mountain hydrologic system: A coupled thermohydrochemical model incorporating buoyant convection, *Water Resour. Res.*, *49*(9), 5880–5899, doi:10.1002/wrcr.20427.

Cheung, W., and H. Rajaram (2002), Dissolution finger growth in variable aperture fractures: Role of the tip-region flow field, *Geophys. Res. Lett.*, *29*(22), 2075, doi:10.1029/2002GL015196.

Cohen, C., D. Ding, M. Quintard, and B. Bazin (2008), From pore scale to wellbore scale: Impact of geometry on wormhole growth in carbonate acidization, *Chem. Eng. Sci.*, *63*, 3088–3099.

Daccord, G. (1987), Chemical dissolution of a porous medium by a reactive fluid, *Phys. Rev. Lett.*, *58*(5), 479–482.

De Waele, J., S.-E. Lauritzen, and M. Parise (2011), On the formation of dissolution pipes in Quaternary coastal calcareous arenites in Mediterranean settings, *Earth Surface Processes and Landforms*, *36*(2), 143–157.

Deng, H., B. R. Ellis, C. A. Peters, J. P. Fitts, D. Crandall, and G. S. Bromhal (2013), Modifications of carbonate fracture hydrodynamic properties by CO_2-acidified brine flow, *Energy Fuels*, *27*(8), 4221–4231.

Detwiler, R. (2010), Permeability alteration due to mineral dissolution in partially saturated fractures, *J. Geophys. Res.*, *115*(9), doi:10.1029/2009JB007206.

Detwiler, R. L., and H. Rajaram (2007), Predicting dissolution patterns in variable aperture fractures: Evaluation of an enhanced depth-averaged computational model, *Water Resour. Res.*, *43*, W04403, doi:10.1029/2006WR005147.

Detwiler, R. L., R. J. Glass, and W. L. Bourcier (2003), Experimental observations of fracture dissolution: The role of Péclet number in evolving aperture variability, *Geophys. Res. Lett.*, *30*(12), 1648, doi:10.1029/2003GL017396.

Dreybrodt, W. (1990), The role of dissolution kinetics in the development of karst aquifers in limestone: A model simulation of karst evolution, *J. Geol.*, *98*, 639–655.

Dreybrodt, W. (1996), Principles of early development of karst conduits under natural and man-made conditions revealed by mathematical analysis of numerical models, *Water Resour. Res.*, *32*, 2923–2935.

Elkhoury, J., R. Detwiler, and P. Ameli (2015), Can a fractured caprock self-heal?, *Earth and Planetary Science Letters*, *417*, 99–106.

Elkhoury, J. E., P. Ameli, and R. L. Detwiler (2013), Dissolution and deformation in fractured carbonates caused by flow of CO_2-rich brine under reservoir conditions, *International Journal of Greenhouse Gas Control*, *16*, S203–S215.

Ellis, B. R., C. A. Peters, J. P. Fitts, G. S. Bromhal, D. McIntyre, R. Warzinski, and E. Rosenbaum (2011), Deterioration of a fractured carbonate caprock exposed to CO_2-acidified brine flow, *Greenhouse Gas. Sci. Technol.*, *1*(3), 248–260.

Ewers, R. O. (1982), Cavern development in the dimensions of length and breadth, PhD thesis, McMaster Univ., Hamilton, Canada.

Falgout, R. D., and U. M. Yang (2002), Hypre: A Library of high performance preconditioners, in *Preconditioners, Lecture Notes in Computer Science*, edited by P. Sloot et. al., pp. 632–641, Springer, Berlin.

Flügel, E. (2004), *Microfacies of Carbonate Rocks: Analysis, Interpretation and Application*, Springer.

Forum, M. P., (1994), MPI: A Message-Passing Interface standard, *Tech. Rep.*, Knoxville, Tenn.

Fredd, C. N., and H. S. Fogler (1998), Influence of transport and reaction on wormhole formation in porous media, *AIChE J.*, *44*, 1933–1949.

García Ríos, M. (2015), Dissolved CO_2 effect on the reactivity of the Hontomín reservoir rocks (limestone and sandstone), PhD thesis, Technical Univ. of Catalonia, Barcelona.

Golfier, F., M. Quintard, and S. Whitaker (2002), Heat and mass transfer in tubes: An analysis using the method of volume averaging, *J. Porous Media*, *5*, 169–185.

Groves, C. G., and A. D. Howard (1994a), Minimum hydrochemical conditions allowing limestone cave development, *Water Resour. Res.*, *30*, 607–615.

Groves, C. G., and A. D. Howard (1994b), Early development of karst systems. I. Preferential flow path enlargement under laminar flow, *Water Resour. Res.*, *30*, 2837–2846.

Hanna, R. B., and H. Rajaram (1998), Influence of aperture variability on dissolutional growth of fissures in karst formations, *Water Resour. Res.*, *34*, 2843–2853.

Hao, Y., M. Smith, Y. Sholokhova, and S. Carroll (2013), Advances in water resources CO_2-induced dissolution of low permeability carbonates. Part II : Numerical modeling of experiments, *Adv. Water Res.*, *62*, 388–408.

Hoefner, M. L., and H. S. Fogler (1988), Pore evolution and channel formation during flow and reaction in porous media, *AIChE J.*, *34*, 45–54.

Howard, A. D., and C. G. Groves (1995), Early development of karst systems. II. Turbulent flow, *Water Resour. Res.*, *31*, 19–26.

Ishibashi, T., T. McGuire, N. Watanabe, N. Tsuchiya, and D. Elsworth (2013), Permeability evolution in carbonate fractures: Competing roles of confining stress and fluid pH, *Water Resour. Res.*, *49*(5), 2828–2842, doi:10.1002/wrcr.20253.

Jamtveit, B., and O. Hammer (2012), Sculpting of rocks by reactive fluids, *Geochemical Perspectives*, *1*(3), 341–481.

Kalia, N., and V. Balakotaiah (2009), Effect of medium heterogeneities on reactive dissolution of carbonates, *Chem. Engineering Science*, *64*(2), 376–390.

Kelemen, P., J. Whitehead, E. Aharonov, and K. Jordahl (1995), Experiments on flow focusing in soluble porous media, with applications to melt extraction from the mantle, *J. Geophys. Res.*, *100*, 475–496.

Krug, J., K. Kessner, P. Meakin, and F. Family (1993), Laplacian needle growth, *Europhys. Lett.*, *24*, 527.

Luquot, L., and P. Gouze (2009), Experimental determination of porosity and permeability changes induced by injection of CO_2 into carbonate rocks, *Chem. Geol.*, *265*(1–2), 148–159.

Luquot, L., O. Rodriguez, and P. Gouze (2014), Experimental characterization of porosity structure and transport property changes in limestone undergoing different dissolution regimes, *Transport in Porous Media*, *101*(3), 507–532.

Maheshwari, P., and V. Balakotaiah (2013), *Comparison of Carbonate HCl Acidizing Experiments With 3D Simulations*, SPE Production and Operations Symposium, vol. 28, Society of Petroleum Engineers, Okla.

Maheshwari, P., R. R. Ratnakar, N. Kalia, and V. Balakotaiah (2013), 3D simulation and analysis of reactive dissolution and wormhole formation in carbonate rocks, *Chem. Eng. Sci.*, *90*, 258–274.

Meakin, P. (1998), *Fractals, Scaling and Growth Far From Equilibrium*, Cambridge Univ. Press.

Meakin, P., and J. Krug (1992), Scaling structure in simple screening models for columnar growth, *Phys. Rev. A*, *46*, 4654–4660.

Noiriel, C., P. Gouze, and B. Made (2013), 3D analysis of geometry and flow changes in a limestone fracture during dissolution, *J. Hydrol.*, *486*, 211–223.

Oltean, C., F. Golfier, and M. A. Bues (2013), Numerical and experimental investigation of buoyancy-driven dissolution in vertical fracture, *J. Geophys. Res. Solid Earth*, *118*(5), 2038–2048, doi:10.1002/jgrb.50188.

Ortoleva, P., J. Chadam, E. Merino, and A. Sen (1987), Geochemical self-organization. II: The reactive-infiltration instability, *Am. J. Sc.*, *287*, 1008–1040.

Ott, H., and S. Oedai (2015), Wormhole formation and compact dissolution in single- and two-phase CO_2-brine injections, *Geophys, Res. Lett.*, *42*, 2270–2276.

Panga, M., M. Ziauddin, and V. Balakotaiah (2005), Two-scale continuum model for simulation of wormhole formation in carbonate acidization, *AIChE J.*, *51*, 3231–3248.

Polak, A., D. Elsworth, J. Liu, and A. S. Grader (2004), Spontaneous switching of permeability changes in a limestone fracture with net dissolution, *Water Resour. Res.*, *40*, W03502, doi:10.1029/2003WR002717.

Rowan, G. (1959), Theory of acid treatment of limestone formations, *J. Inst. Pet.*, *45*(431), 321.

Saupe, D. (1988), *Algorithms for random fractals*, 71–136, edited by H. Peitgen and D. Saupe, Springer, New York.

Smith, M., Y. Sholokhova, Y. Hao, and S. Carroll (2013), CO_2-induced dissolution of low permeability carbonates. Part I: Characterization and experiments, *Adv. in Water Resour.*, *62*, 370–387.

Spiegelman, M., P. Kelemen, and E. Aharonov (2001), Causes and consequences of flow organization during melt transport: The reaction infiltration instability in compactable media, *J. Geophys. Res.*, *106*, 2061–2077.

Stanley, H. E., and N. Ostrowsky (1988), Proc. NATO Advanced Study Institute, NATO Advanced Science Institute Series E: Applied Sciences, Random fluctuations and pattern growth, *157*, Kluwer Academic Publishers, Hingham, Mass.

Szymczak, P., and A. J. C. Ladd (2006), A network model of channel competition in fracture dissolution, *Geophys. Res. Lett.*, *33*, L05401, doi:10.1029/2005GL025334.

Szymczak, P., and A. J. C. Ladd (2009a), Wormhole formation in dissolving fractures, *J. Geophys. Res.*, *114*, B06203, doi:10.1029/2008JB006122.

Szymczak, P., and A. J. C. Ladd (2009b), Comment on: "From pore scale to wellbore scale: Impact of geometry on wormhole growth in carbonate acidization by C.E. Cohen et al. [Chemical Engineering Science 63, 3088-3099, 2008]", *Chem. Eng. Sci.*, *64*(12), 3029–3030.

Szymczak, P., and A. J. C. Ladd (2011a), The initial stages of cave formation: Beyond the one-dimensional paradigm, *Earth Planet. Sci. Lett.*, *301*, 424–432.

Szymczak, P., and A. J. C. Ladd (2011b), Instabilities in the dissolution of a porous matrix, *Geophys. Res. Lett.*, *38*, L07403, doi:10.1029/2011GL046720.

Szymczak, P., and A. J. C. Ladd (2012), Reactive infiltration instabilities in rocks. Fracture dissolution, *J. Fluid Mech.*, *702*, 239–264.

Szymczak, P., and A. J. C. Ladd (2013), Interacting length scales in the reactive-infiltration instability, *Geophys. Res. Lett.*, *40*, 3036–3041.

Szymczak, P., and A. J. C. Ladd (2014), Reactive infiltration instabilities in rocks. Part 2: Dissolution of a porous matrix, *J. Fluid Mech.*, *738*, 591–630.

White, W. B., and J. Longyear (1962), Some limitations on speleogenetic speculation imposed by the hydraulics of groundwater flow in limestone, *Nittany Grotto Newl.*, *10*, 155–167.